

SliceGraph: Mapping Process Isomers in Multi-Run Chain-of-Thought Reasoning

Kang Chen^{1*}, Junjie Nian^{1*}, Yixin Cao^{1,2†}, Yugang Jiang¹

¹Fudan University, ²Shanghai Innovation Institute

Abstract

Multi-run chain-of-thought reasoning is usually collapsed to final-answer aggregates, which discard how sampled trajectories share, split, and rejoin through intermediate computation. We propose **SliceGraph**, a post-hoc problem-model-cell graph built by mutual- k NN over sparse activation-key Jaccard similarity between CoT slices, and treat it as a *measurement object* for process geometry rather than as a decoding program. Across sampled CoT ensembles from three primary 4B/8B models on math and science benchmarks, blinded annotation supports SliceGraph biconnected components as shared reasoning-state units and process families as within-family strategy-coherent route units. In 85.5% of 954 problem-model cells, correct CoTs sharing the same normalized answer split into multiple process families; among cells with at least two such runs, 76.6% of run pairs are cross-family on average. We call such same-answer, family-divergent correct trajectories *process isomers*. A label-seeded reward field provides a separate value-landscape layer: success-associated regions often split into disconnected high-value cores, and route families specialize over these core footprints rather than merely duplicating one another. A typed-state transition analysis further shows that process families navigate the same atlas with distinct transition kernels under matched null controls. Representation ablations, a cross-architecture replication, and two cross-scale replications support the robustness of the route-family scaffold, showing that final-answer aggregation overlooks this structured multi-route process geometry.

Correspondence: yxcao@fudan.edu.cn

Code: <https://github.com/JunjieNian/SliceGraph>

1 Introduction

Test-time sampling now routinely draws many CoT trajectories per problem [2, 8, 11, 14], while self-consistency aggregates them only by final string. But the N runs of one problem-model cell are not a bag of independent samples: they share intermediate computation, fork at decision points, and rejoin through common subroutines. Once internal states are connected by similarity, consistency can be lifted from final answers to *processes*, and two correct runs are consistent when they reach overlapping computation. Most internal analyses so far remain within-run, studying semantic convergence, step-specific geometry, or late correctness signals [9, 12] rather than the joint structure across runs.

Building such a graph requires slice-level similarity, for whole-run is too coarse: two runs can share a long

* Contributed equally.

† Corresponding author.

trunk and diverge at one fork, or reach the same answer by different routes. Once the graph is built, the substantive question shifts from selection to geometry. When many CoTs solve the same problem, do correct solutions converge to one process route, or do they form several distinct *process isomers* that share the same final answer through different intermediate routes?

Prior graph and topology pipelines on traces [10, 13, 18] compress each slice via PCA, UMAP, or sentence transformers before reading similarities. In our fixed mutual- k NN scaffold, however, projection- or text-based slice representations distort the route geometry: PCA compresses correct-only family counts and slice-text embeddings nearly collapse the atlas (Section 4.3). Unprojected sparse activation-key Jaccard similarity preserves the multi-route structure across all three primary models.

We therefore build directly on top- k activation key sets. Each slice is a bounded binary key set, and per-problem edges are mutual- k NN under Jaccard distance. We call this object **SliceGraph** and treat it as a measurement target, not a decoding program. Biconnected components, articulation points, and process families are structural units read from this fixed graph. Reward diffusion and typed-state transition diagnostics then add label and temporal information on top of the same scaffold. Two blinded annotation studies validate the structural object before any geometric claim is made, and matched null controls test which claims survive after graph structure, family labels, answer labels, or temporal order are perturbed. Informally, two correct runs that reach the same answer through different process families are *process isomers*: same problem, same normalized answer, different route scaffold. Process isomerism is a route relation, not a value relation: high-value cores can refine, explain, or separate route families, but they do not define whether two same-answer traces are isomers. High-value cores then show whether those routes traverse shared or disjoint value basins.

Contributions.

- **A process atlas for mapping same-answer route diversity.** We introduce SliceGraph, a post-hoc per-problem-model-cell graph built directly from sparse activation-key overlap between CoT slices. Unlike decoding graphs, SliceGraph is a measurement object: it exposes shared trunks, forks, partial rejoin points, and route-level structure after sampling.
- **Validated structural units.** We decompose SliceGraph into biconnected components, articulation points, process families, and label-seeded high-value cores. Blinded annotation supports BCCs as shared reasoning-state units and process families as within-family strategy-coherent route units; robustness checks test representation choice, graph perturbations, family-label shuffles, answer-label shuffles, and temporal-order perturbations.
- **Process isomers behind the same answer.** On the validated atlas, sampled correct CoTs often reach the same normalized answer through different correct-only process families. We define these family-divergent same-answer traces as process isomers. High-value cores provide a separate value-landscape layer, showing that success-associated regions are often multi-basin and that route families specialize over those basins.
- **Route dynamics, not just route labels.** We lift block trajectories to a typed-state transition model and show that family-specific transition kernels differ significantly under matched null controls.

2 Related Work

Graphs as inference programs versus measurement objects. Self-consistency [11], Tree-of-Thoughts [14], and Graph-of-Thoughts [2] use graphs as decoding strategies built before or during sampling. Our graph is

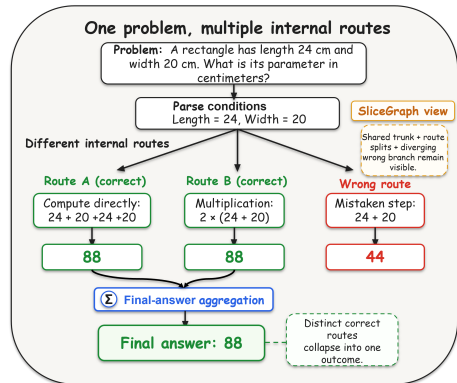


Figure 1 Same-answer runs can follow distinct process families.

instead a *measurement* object: it is built after sampling from local activation similarity across many runs, and is used to characterise process geometry rather than to drive decoding.

Within-run trajectory analysis. A line of work analyses LLM reasoning as structured motion in representation space, including semantic convergence from truncated trajectories [12], step-specific geometry [9], layer-wise displacement of the truth signal [6], hidden-state DAG probes [17], and shared decision pivots [5]. These analyses stay within a single trajectory; we study the joint neighbourhood structure across runs for one problem.

Graph and topology pipelines. The graph and topology pipelines we compare against rely on intermediate projection: Mapping the Minds [13] clusters CoT paragraphs into NLI dependency graphs, Landscape of Thoughts [18] projects answer-distance vectors with t -SNE, and The Shape of Reasoning [10] runs persistent homology on step embeddings. Activation-set similarity has been used as a best-of- N selector in Neuron Agreement Decoding [3]; the same sparse-cache infrastructure supports temporal explore-exploit phase detection for label-free CoT scoring [4]. Building on these, we construct the graph directly on unprojected sparse activation-key Jaccard with no projection or sentence embedding and then analyse its combinatorial topology; Section 4.3 shows that PCA and sentence-embedding pipelines on the same scaffold compress the multi-route family geometry that SliceGraph captures.

3 Method

The method has five layers. The first three build the route scaffold on which process isomerism is measured without the label-seeded reward field; the last two add value-landscape and temporal information on top of that fixed scaffold. Graph topology, BCC membership, and correct-run co-visitation families do not use the reward field; role labels are interpretive overlays that may use final-answer purity but do not define process families or process isomers. Section 3.1 builds the graph from sparse activation slices. Section 3.2 decomposes it into biconnected components and assigns roles, giving the structural units later validated in Section 4.2. Section 3.3 clusters runs into process families and introduces the *process isomer* relation that organises the multi-route geometry of Section 4.4. Section 3.4 defines the label-seeded reward field and the high-value-core mask, and Section 3.5 lifts each run to a typed-state transition model whose family-specific kernels anchor Section 4.6. All main analyses operate on non-trivial regions only.

3.1 SliceGraph construction

For each problem-model cell we sample $N=64$ separately sampled CoT runs from a precomputed sparse activation cache. Each *neuron* is a (layer, unit) pair indexed by a 32-bit key, and the active set at a given token is the top-ranked MLP neurons by the positive part of the post-gating intermediate (Appendix A.2). We first aggregate activations into 32-token rows, then aggregate every consecutive `sep_up` rows into one coarser reasoning slice; at the canonical `sep_up=8`, a graph node therefore summarises a 256-token segment. Magnitudes are discarded after retaining the most-active keys, so each analysed slice is a binary key set $\mathcal{K}_{r,t}$ with no projection or text-embedding step.

We connect two slices by their Jaccard overlap, $d_J(i, j) = 1 - |\mathcal{K}_i \cap \mathcal{K}_j|/|\mathcal{K}_i \cup \mathcal{K}_j|$, and keep an undirected edge *iff* the relation is mutual in the top- k neighbourhood, weighting edges by an RBF kernel of d_J . The resulting graph \mathcal{G} has nodes indexed by run and coarse position, with edges encoding cross-run local similarity on a single problem. The neighbourhood parameter k controls only how many local neighbours are eligible before the mutuality filter. Exact cache constants, kernel scale, and size cap are in Appendix A.2; sensitivity sweeps are in Appendices B.1 and B.6.

3.2 Biconnected-component decomposition and non-trivial regions

We treat \mathcal{G} as a graph of *shared slice-level computation*. A *biconnected component* (BCC) is a maximal subgraph that stays connected after removing any single node, and so groups slices that are mutually reachable through

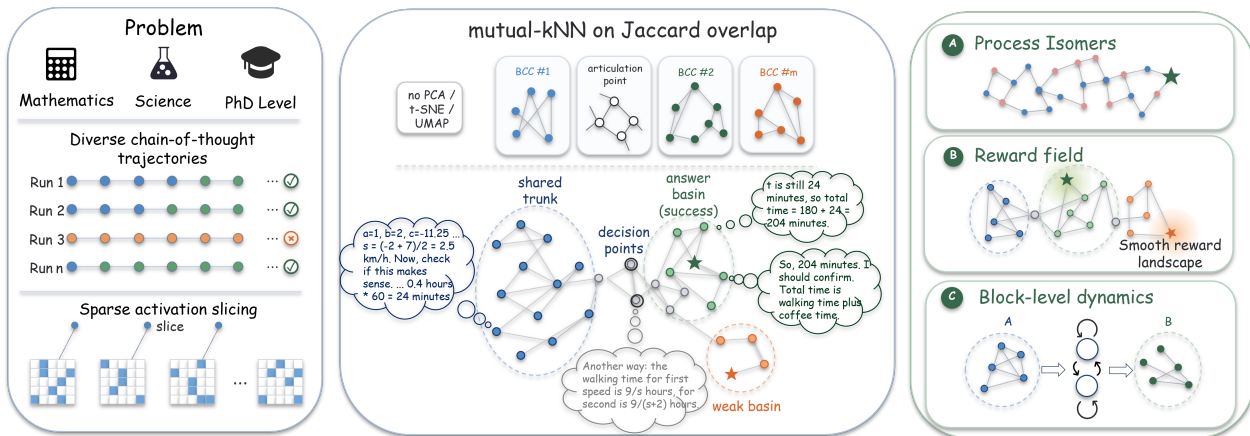


Figure 2 SliceGraph pipeline. SliceGraph turns many sampled CoTs for one problem-model cell into an activation-key atlas. Process families are structural units read from the fixed graph; label-seeded high-value cores and family-specific navigation kernels add answer labels and temporal transitions on top of that scaffold.

redundant paths. An *articulation point* between two BCCs is a *branch point* where the reasoning population forks. We decompose \mathcal{G} component-wise into BCCs and split the result into trivial K_2 bridges and non-trivial $|b| \geq 3$ blocks. No largest-connected-component filter is applied: disconnected components remain eligible, while K_2 bridges are retained as connectors but are not treated as semantic regions. Sensitivity to this convention is reported in Appendix B.1.

We then assign each block one of five roles, namely `SHARED_TRUNK`, `ANSWER_BASIN`, `WEAK_BASIN`, `DECISION_POINT`, or `INTERMEDIATE`, based on its run coverage, size, dominant-answer purity, and median position. The explicit thresholds and bridge-versus-cycle formulation are in Appendix A.3; role sensitivity is in Appendix B.1. The correspondence between these units and human notions of shared reasoning state is validated in Section 4.2; the same units support the family geometry, label-seeded solution landscape, and navigation analyses that follow.

3.3 Process families and process isomers

Two runs that visit similar sets of regions are likely to share a route footprint, and may correspond to the same high-level strategy. We turn this intuition into a clustering by reducing each run to the set of non-trivial blocks it visits across all analysed slices, $\mathcal{S}_r = \bigcup_t C_{r,t}^{\text{nt}}$, and forming a weighted Jaccard with rare-block upweighting $\omega_b = 1/\max(c_b, 0.01)$, where c_b is the fraction of runs reaching block b :

$$J(r, r') = \frac{\sum_{b \in \mathcal{S}_r \cap \mathcal{S}_{r'}} \omega_b}{\sum_{b \in \mathcal{S}_r \cup \mathcal{S}_{r'}} \omega_b}. \quad (1)$$

Repeated visits are discarded, since families are meant to capture which regions are visited rather than how long a run dwells in them. After block-coverage weights are fixed from the full cell, all headline correct-family statistics construct this run-level co-visitation graph on normalized-correct runs only, keep edges with $J \geq 0.05$, and partition it by Louvain community detection at resolution 1.0 and seed 42. Incorrect runs are used to define full-cell block coverage, the reward field, and visual overlays, but they are not nodes in the correct-only Louvain partition. Whether two runs placed in the same family are also judged by humans to use the same strategy is the second annotation study of Section 4.2. These families anchor the *process isomer* relation:

Definition 1 (Process isomer). *Two correct CoT runs r, r' for the same problem-model cell are process isomers if they reach the same normalized final answer and are placed in different correct-only process families under the weighted-Jaccard Louvain partition above.*

High-value cores introduced next (Section 3.4) serve as a value-landscape refinement rather than a second isomer criterion.

3.4 Label-seeded reward field and high-value cores

Families capture which regions a run visits but not which regions belong to the shared solution landscape. The reward field is not used to discover process families and is not treated as an online correctness predictor; it is a label-seeded explanatory field used only after the graph and correct-family partition are fixed. For a block b visited by runs \mathcal{R}_b , the global seed is a support-shrunk excess success rate,

$$v_b^{(0)} = \mathbf{1}[3 \leq n_b \leq n-3] \left(\frac{1}{n_b} \sum_{r \in \mathcal{R}_b} y_r - \frac{1}{n} \sum_r y_r \right) \left(\frac{n_b}{n} \right)^{1/2}, \quad n_b = |\mathcal{R}_b|. \quad (2)$$

We then diffuse this seed over a row-normalized block matrix \mathbf{P} that combines self-loops, block-cut adjacency, and binarized symmetrized temporal transitions:

$$\mathbf{v}^{(t+1)} = \alpha \mathbf{v}^{(0)} + (1-\alpha) \mathbf{P} \mathbf{v}^{(t)}, \quad (3)$$

with $\alpha=0.65$ for 24 PageRank-style steps. The run-level leave-one-out variant, support thresholds, and full adjacency construction are in Appendix C. The *high-value core* C is the top quartile of strictly-positive field values on $\mathbf{v}^{(24)}$, and serves as the label-seeded geometry analysed in Section 4.5. When C splits into several connected components the cell is *multi-core*, giving a value-landscape divergence layer complementary to the family partition.

Section 4.5 uses specialization and coverage loss as primary alignment readouts, and reports field sharpness as a secondary diagnostic, each with its natural denominator. *Family-core footprint specialization* asks whether each correct-only family concentrates its visited-block footprint on a subset of high-value-core components. *Field sharpness* is the ratio between the maximum of a family-conditioned reward field and the maximum of the pooled reward field. *Block-coverage loss* removes a family and measures the drop in the union of visited non-trivial blocks; the population readout uses the most coverage-critical family per cell. For $K \geq 2$ high-value-core components, we write $p_f(k) \propto |B_f \cap C_k|/|C_k|$ for family f 's normalized core-footprint distribution and report

$$\text{Spec} = 1 - \frac{1}{|F_+|} \sum_{f \in F_+} \frac{H(p_f)}{\log K}, \quad (4)$$

where F_+ are families with non-zero core footprint; thus 0 means diffuse family footprints and 1 means component-specific footprints.

Core divergence. For reward-evaluable cells, two correct runs are *core-divergent* if their non-empty sets of visited high-value-core components are disjoint. This relation characterizes value-landscape divergence rather than defining the primary route partition; it is evaluated only for runs with at least one high-value-core visit.

3.5 Family-specific typed-state dynamics

To analyse navigation, we lift each run's block trajectory to a typed-state transition chain $z_{r,t} = (\text{role}(b_{r,t}^*), \text{posbin}(\tau_t), \text{core}(b_{r,t}^*))$, where $b_{r,t}^*$ is the primary non-trivial block at slice t and $\tau_t \in [0, 1]$ is the normalized within-run position binned into early, mid, and late thirds. The state alphabet deliberately includes the high-value-core indicator: dynamics are estimated by process family, but the states record whether a route is inside or outside the label-seeded value landscape. Slices with no non-trivial block are skipped before compaction; consecutive duplicate typed states are merged, absorbing correct/wrong terminals are appended, and Laplace-smoothed family kernels P_f are estimated from compacted transition

counts C_{ij}^f :

$$P_f(i, j) = \frac{C_{ij}^f + \alpha_{\text{smooth}}}{\sum_{j'} C_{ij'}^f + \alpha_{\text{smooth}}|\mathcal{S}|}, \quad \alpha_{\text{smooth}}=0.5. \quad (5)$$

The population diagnostic is row-averaged total variation,

$$\text{TV}(P_f, P_{f'}) = \frac{1}{2|\mathcal{S}|} \sum_{i \in \mathcal{S}} \|P_f(i, \cdot) - P_{f'}(i, \cdot)\|_1, \quad (6)$$

where \mathcal{S} follows the released state alphabet; Appendix C details the absorbing-terminal convention. Companion navigation diagnostics are defined in Appendix C and are used only for case-level inspection.

SliceGraph is evaluated as a measurement object for process geometry and process-isomer structure; using it inside decoding is left for future work.

4 Experiments

4.1 Setup

We evaluate SliceGraph on five math and science reasoning benchmarks: AIME24 [15], AIME25 [16], BRUMO25 and HMMT25 from MathArena [1], and GPQA Diamond [7]. The primary corpus uses three 4B and 8B models sampled with chain-of-thought prompting: DeepSeek-R1-0528-Qwen3-8B (**R1-8B**), Qwen3-4B-Thinking-2507 (**Think**), and Qwen3-4B-Instruct-2507 (**Inst**), all run at the canonical configuration. The primary corpus contains 60,622 graph-valid analysed trajectories from 61,052 sampled runs across 954 problem-model cells, corresponding to 318 unique benchmark problems each evaluated under the three primary models at $N=64$ runs per cell. Run-number sensitivity suggests that $N=64$ retains 95.0% of the process-family coverage observed on deeper $N=256$ caches (Appendix B.1). Subsampling curves further show that block coverage is near saturation around $N \approx 32$, while family and high-value-core counts keep growing as rare-block neighbourhoods enter the sample. We run a cross-architecture replication on DeepSeek-R1-Distill-Llama-8B (**Llama-8B**), a within-family cross-scale replication on Qwen3-32B (**Qwen3-32B**), and a cross-generation cross-scale replication on the math-specialized Qwen2.5-Math-72B-Instruct (**Q2.5-72B**), with per-model results in Appendices E.3, E.2, and E.1. Effect sizes and uncertainty conventions are detailed in Appendix A.4. The reward, multi-core, typed-state, and family-TV analyses use progressively stricter subsets carved from the canonical 954 problem-model cells, with the filtering chain in Appendix A.1. Correctness and same-answer membership are evaluated after benchmark-specific answer normalization, and process-isomer comparisons are made only within the normalized correct-answer class.

We organise the experiments as a validity ladder: semantic validation (§4.2), representation preservation (§4.3), family-defined process-isomer geometry (§4.4), label-seeded value-landscape refinement (§4.5), and value-aware isomer dynamics (§4.6).

Each RQ is paired with a targeted control: human annotation for graph-unit semantics, representation ablations for scaffold choice, pairwise and split-half diagnostics for process isomers, reward-core alignment readouts for the value landscape, and family-label/common-support nulls for navigation dynamics (Table 15 in the appendix).

4.2 RQ1. Are the graph units semantic?

Before reading geometry off the graph, we ask whether its two discovered units, namely biconnected components and process families, line up with human notions of shared thinking and shared strategy. We answer this with two blinded annotation studies, each run by two independent annotators on matched within-unit and across-unit pairs. Both studies support the semantic interpretation.

Biconnected components correspond to shared reasoning state. We constructed 72 blinded slice-text pairs, half within the same BCC and half length-matched across BCCs, and asked two independent annotators to judge whether the two slices represent the same reasoning operation under matched strict execution-level rubrics. Annotator A matches the within/across-BCC labels on 88.9% of pairs and Annotator B on 90.3%; cross-annotator agreement is $\kappa=0.97$ on the $n=71$ decisive pairs. The annotation protocol and agreement statistics are reported in Appendices D.2 and D.3.

Process families are within-family strategy-coherent. A separate 77-pair pack drawn from 8 problems, with 46 within-family and 31 length-matched across-family pairs, asked whether two runs use the same high-level strategy. Within-family pairs reproduce the same-strategy judgement in 94.4% of decisive cases; cross-annotator agreement on the across-family slice is $\kappa=0.74$ with 81.8% overall decisive exact agreement (Appendix D.4). Across-family separation is partial at 47.6% different-strategy rate; families capture finer-grained process differences than “high-level strategy,” so we use *process isomer* at the route-family granularity. Task B should therefore be read as validating within-family coherence rather than perfect separation of human-named strategies. Across-family pairs can still share a textbook strategy, because SliceGraph families are defined at a finer route-footprint granularity; hence *process isomerism* denotes different graph-measured process routes, not necessarily different human solution templates.

4.3 RQ2. Does the activation-key scaffold preserve process geometry?

If the scaffold distorts process geometry, the isomer and dynamics claims that follow are built on artefactual structure. We hold the mutual- k NN framework, BCC decomposition, and family construction fixed and vary only the slice representation, evaluating each by two criteria: whether it yields a valid non-trivial BCC scaffold, and whether the resulting family geometry preserves the canonical multi-route multiplicity.

Evidence. Under the fixed scaffold, activation-key Jaccard preserves the highest and most stable correct-family multiplicity across primary models (Table 1; per-model breakdown in Appendix B.2). Cosine and overlap on the same sparse keys are close, supporting the activation-key object rather than a single metric artefact. PCA-50 remains graph-valid but compresses family counts by ~ 1 per cell, while slice-level MiniLM nearly collapses the atlas: only 21/954 cells yield a valid decomposition, with at most 11 valid cells for any primary model.

Table 1 Representation ablation under a fixed mutual- k NN scaffold. Multi-fam rate / mean correct families per valid cell. Canonical rows evaluate all 954 cells; collapsed representations report their valid-cell counts (see Appendix B.2).

Scaffold representation	R1-8B	Think	Inst
Activation keys, Jaccard (ours)	89.3/5.14	86.2/4.61	81.1/4.21
Activation keys, cosine	88.1/4.80	85.5/4.36	79.6/3.87
PCA-50 + cosine	81.4/3.38	81.4/3.33	73.8/3.00
MiniLM slice-text	<i>collapsed (21/954 valid cells; ≤ 11 per model)</i>		

PCA preserves an activation-based object but compresses set-overlap contrast; MiniLM collapses because same-problem topical similarity saturates execution-level contrast. The unprojected activation-key scaffold therefore occupies the narrow band between collapse and over-fragmentation that preserves the route structure validated in RQ1, and we use Jaccard as the canonical metric.

4.4 RQ3. Are same-answer correct CoTs route-isomeric?

Process isomerism is a family-defined relation (Definition 1): two correct runs are isomers when they reach the same normalized answer but belong to different correct-only process families. We first establish how prevalent this relation is using only the family partition; the reward field and typed-state dynamics are layered on in §4.5–§4.6. Figure 3 visualises three layers of one atlas; Figure 4 gives population diagnostics and Table 2 per-model breakdowns.

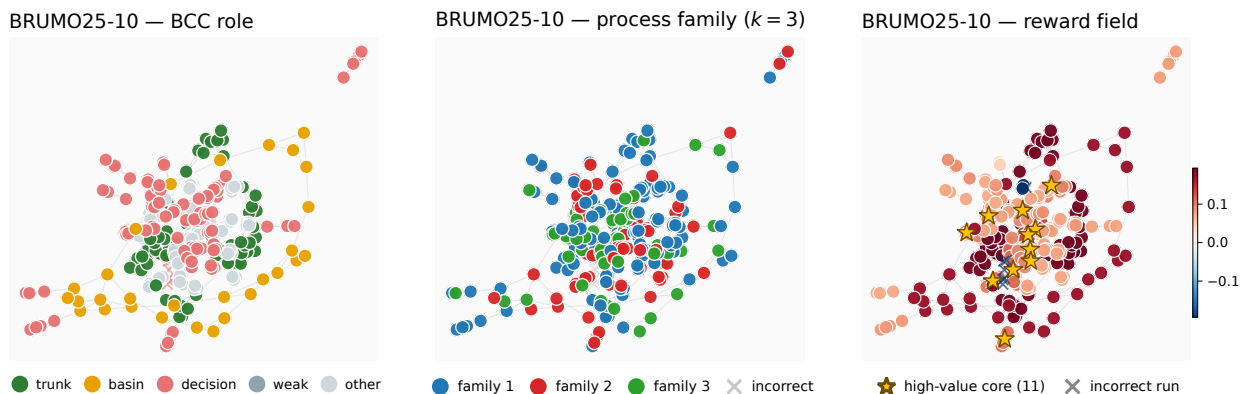


Figure 3 Three readouts of a single SliceGraph for BRUMO25-10 (Inst, 64 runs, 60 correct). Every node is one CoT slice; 273 slices in non-trivial biconnected components are shown, with trivial K_2 bridge components omitted. **Left:** BCC block-type role (trunk, basin, decision, weak, other). **Middle:** correct-only process families ($k=3$ families; \times = incorrect runs). **Right:** propagated reward field seeded by per-block correctness deviation; \star marks the centroid of each high-value-core component (11 cores). Note that family colours and core locations split differently, illustrating that route families and value cores are related but non-identical layers.

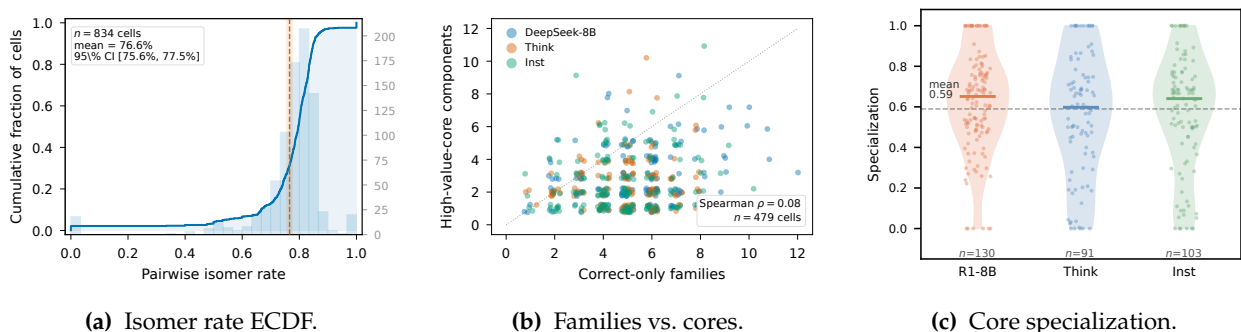


Figure 4 RQ3/RQ4 population geometry. (a) ECDF of pairwise family-isomer rates over 834 cells; vertical lines mark the bootstrap 95% CI. (b) Correct-family count vs. core components on 479 reward-evaluable cells (Spearman $\rho=0.08$): the two layers are non-redundant in count. (c) Family-core specialization on 324 multi-core cells (bars = medians): despite weak count correlation, families spatially specialize over distinct core footprints (pooled mean = 0.59).

Route multiplicity. Before introducing the reward field, 85.5% of the 954 canonical cells contain more than one correct-only process family. At the pair level, 76.6% of normalized-correct run pairs are family-isomeric on average, with a problem-clustered bootstrap 95% CI of [75.6, 77.5]% (Figure 4a).

Sampling robustness. Split-half resampling preserves the signal on a stricter split-valid subset: both halves are multi-family in 97.2% of cells ($n=779$). A held-out atlas built from 32 train runs and projected onto 32 test runs retains 91% multi-family cells; fixing the correct-run count to $m=4$ still yields 58% isomer rate (Appendices B.4, B.5). A resolution \times threshold sweep confirms stability (Appendix B.6). Low-isomer cells remain, and SliceGraph recovers multi-route structure when present rather than forcing it. The signal is not driven by bridge-like length fragmentation: including K_2 bridges barely changes the multi-family rate (85.5% \rightarrow 86.8%) but overfragments the partition, inflating mean families from 4.66 to 11.27 and raising the between-family length-variance ratio from 0.46 to 0.70 (Appendix B.1). Thus, the same correct answer is usually not a single route endpoint but a set of graph-separated route footprints.

Table 2 Dataset-level route multiplicity for the primary corpus. Entries: % cells with ≥ 2 correct-only families / mean correct families. Full six-model breakdown including replication models in Table 10.

Model	AIME24	AIME25	BRUMO25	GPQA	HMMT25	All
R1-8B	86.7 / 4.87	86.7 / 4.80	86.7 / 4.57	92.4 / 5.50	76.7 / 3.97	89.3 / 5.14
Think	93.3 / 5.07	86.7 / 5.10	96.7 / 4.77	85.9 / 4.60	70.0 / 3.57	86.2 / 4.61
Inst	83.3 / 4.20	70.0 / 3.43	76.7 / 3.70	87.9 / 4.72	50.0 / 2.17	81.1 / 4.21

4.5 RQ4. How do route isomers align with the label-seeded value landscape?

We now add the reward field (§3.4) as a value contour over the route atlas. With the correct-only family partition fixed, the field marks where correctness-associated mass concentrates after label-seeded diffusion. The question shifts from route multiplicity to route–value alignment: do same-answer families share one high-value component, or specialize over multiple? Core counts are treated as descriptive geometry; label-permutation stress tests are in Appendix C.4.

Table 3 Value-landscape readouts for RQ4. The first three rows test non-redundancy between route families and high-value cores; the last three test spatial alignment and coverage.

Readout	Value	Subset
Multi-core rate	67.6%	479 reward-evaluable
2nd / 1st core size	0.54	324 multi-core
Family–core count ρ	0.08	479 reward-evaluable
Specialization	0.59	324 multi-core
Coverage loss > 10%	94.5%	816 multi-family
Core-divergence uplift	+1.3 pp	834 isomer-eligible

Evidence. Of 479 reward-evaluable cells, 324 are multi-core (Table 3), with mean second-to-first core size ratio 0.54. This value granularity is not a relabelling of route multiplicity, since family and core component counts correlate weakly (Figure 4b). Yet they align spatially (Figure 4c)—families specialize over distinct core footprints and are individually coverage-critical—while a disjoint-core criterion adds only 1.3 pp beyond the family-isomer relation. High-value cores therefore refine the route map without redefining process isomerism.

4.6 RQ5. Do process isomers navigate the atlas differently?

The value layer shows where route families concentrate; it does not yet say whether they traverse the atlas differently. We turn the same atlas into a typed-state traffic model (§3.5), estimating one transition kernel per family and comparing between-family TV to a size-preserving label-shuffle null. Common-support TV restricts rows to states visited by both families, ruling out disjoint support; Figure 5 shows both diagnostics.

Family-specific kernels carry route-specific signal. On the 403-cell core-eligible multi-family subset, row-averaged TV exceeds the label-shuffle p_{95} in **80.9%** of cells (median $z=3.14$). The result is not just a static-footprint effect: family-TV is weakly correlated with footprint specialization (Pearson -0.07). Nor is it explained only by disjoint support: common-support TV preserves the direction: **77.4%** of cells exceed matched p_{95} , with median $z=3.45$ and median 7 shared typed states per family pair. Thus families differ not only in where they concentrate but also in how they move through the typed-state atlas. Appendix C.4, C.5 give stress tests and null details; .

Cross-model replication across RQ3–RQ5. Llama-8B tests architecture transfer, Qwen3-32B within-family scaling, and Q2.5-72B saturation. Llama-8B and Qwen3-32B match the route-family, value-landscape, and family-TV pattern; Q2.5-72B attenuates multiplicity but retains the qualitative geometry on unsaturated GPQA (Appendices E.3, E.2, E.1).

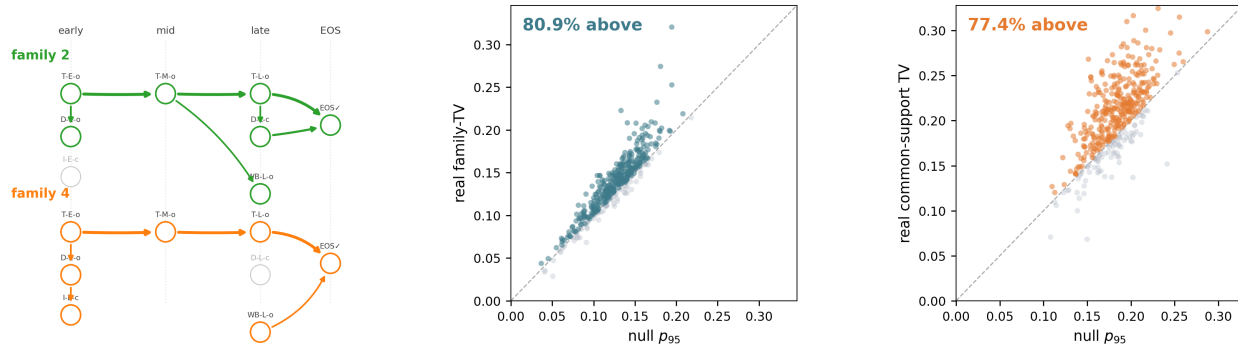


Figure 5 Family-specific typed-state dynamics. (a) Two families share a typed-state vocabulary but place different transition mass. (b, c) Real family-TV and common-support TV versus size-preserving label-shuffle p_{95} ; points above the diagonal exceed the matched null.

5 Conclusion

SliceGraph is a post-hoc measurement atlas, not a decoder: it maps sparse neuron-activation keys from multi-run CoTs into a graph of shared and diverging process routes. On this activation-key atlas, same-answer correct CoTs are often process-isomeric. High-value cores and family-specific kernels further show how route families align with value basins and differ in navigation dynamics. Together, validated graph units, activation-key scaffolds, reward-field-free isomer statistics, value-layer refinement, and null-controlled dynamics reveal non-monolithic same-answer reasoning.

6 Limitations and broader impact

SliceGraph inherits the limits of observational activation analysis: it requires hooks and cached sparse activations, depends on slice/block conventions, and may under-sample rare routes because annotations and long-tail transitions are finite. Its label-seeded reward field is descriptive, so label permutations are stress tests of that layer rather than one-sided nulls for multi-core counts (Appendix C.4). Claims are scoped to non-code math/science; code-generation tasks may differ. Broader impacts are diagnostic: SliceGraph can audit route diversity, collapse, and over-concentration, but selection or early-stopping use could amplify sampling biases or suppress rare correct routes.

References

- [1] Mislav Balunović, Jasper Dekoninck, Ivo Petrov, Nikola Jovanović, and Martin Vechev. MathArena: Evaluating LLMs on uncontaminated math competitions. *arXiv preprint arXiv:2505.23281*, 2025. doi: 10.48550/arXiv.2505.23281. URL <https://arxiv.org/abs/2505.23281>.
- [2] Maciej Besta, Nils Blach, Aleš Kubicek, Robert Gerstenberger, Michał Podstawski, Lukas Gianinazzi, Joanna Gajda, Tomasz Lehmann, Hubert Niewiadomski, Piotr Nyczyk, and Torsten Hoefler. Graph of thoughts: Solving elaborate problems with large language models. In *Proceedings of the AAAI Conference on Artificial Intelligence*, volume 38, pages 17682–17690, 2024. doi: 10.1609/aaai.v38i16.29720. URL <https://ojs.aaai.org/index.php/AAAI/article/view/29720>.
- [3] Kang Chen, Yaoning Wang, Kai Xiong, Zhuoka Feng, Wenhe Sun, Haotian Chen, and Yixin Cao. Do LLMs signal when they’re right? evidence from neuron agreement. *arXiv preprint arXiv:2510.26277*, 2025. doi: 10.48550/arXiv.2510.26277. URL <https://arxiv.org/abs/2510.26277>.
- [4] Kang Chen, Zhuoka Feng, Sihan Zhao, Kai Xiong, Junjie Nian, Yaoning Wang, Changyi Xiao, and Yixin Cao. NEX: Neuron explore–exploit scoring for label-free chain-of-thought selection and model ranking. *arXiv preprint arXiv:2602.05805*, 2026. doi: 10.48550/arXiv.2602.05805. URL <https://arxiv.org/abs/2602.05805>.
- [5] Dongkyu Cho, Amy B. Z. Zhang, Bilel Fehri, Sheng Wang, Rumi Chunara, Hengrui Cai, and Rui Song. Correct reasoning paths visit shared decision pivots. *arXiv preprint arXiv:2509.21549*, 2025. doi: 10.48550/arXiv.2509.21549. URL <https://arxiv.org/abs/2509.21549>.
- [6] Hamed Damirchi, Ignacio Meza De la Jara, Ehsan Abbasnejad, Afshar Shamsi, Zhen Zhang, and Javen Shi. Truth as a trajectory: What internal representations reveal about large language model reasoning. *arXiv preprint arXiv:2603.01326*, 2026. doi: 10.48550/arXiv.2603.01326. URL <https://arxiv.org/abs/2603.01326>.
- [7] David Rein, Betty Li Hou, Asa Cooper Stickland, Jackson Petty, Richard Yuanzhe Pang, Julien Dirani, Julian Michael, and Samuel R. Bowman. GPQA: A graduate-level google-proof Q&A benchmark. *arXiv preprint arXiv:2311.12022*, 2023. doi: 10.48550/arXiv.2311.12022. URL <https://arxiv.org/abs/2311.12022>.
- [8] Charlie Victor Snell, Jaehoon Lee, Kelvin Xu, and Aviral Kumar. Scaling LLM test-time compute optimally can be more effective than scaling parameters for reasoning. In *The Thirteenth International Conference on Learning Representations*, 2025. URL <https://openreview.net/forum?id=4FWAwZtd2n>.
- [9] Lihao Sun, Hang Dong, Bo Qiao, Qingwei Lin, Dongmei Zhang, and Saravan Rajmohan. LLM reasoning as trajectories: Step-specific representation geometry and correctness signals. *arXiv preprint arXiv:2604.05655*, 2026. doi: 10.48550/arXiv.2604.05655. URL <https://arxiv.org/abs/2604.05655>.
- [10] Xue Wen Tan, Nathaniel Tan, Galen Lee, and Stanley Kok. The shape of reasoning: Topological analysis of reasoning traces in large language models. *arXiv preprint arXiv:2510.20665*, 2025. doi: 10.48550/arXiv.2510.20665. URL <https://arxiv.org/abs/2510.20665>.
- [11] Xuezhi Wang, Jason Wei, Dale Schuurmans, Quoc V. Le, Ed H. Chi, Sharan Narang, Aakanksha Chowdhery, and Denny Zhou. Self-consistency improves chain of thought reasoning in language models. In *The Eleventh International Conference on Learning Representations*, 2023. URL <https://openreview.net/forum?id=1PL1NIMMrw>.
- [12] Zihao Wei, Liang Pang, Jiahao Liu, Wenjie Shi, Jingcheng Deng, Shicheng Xu, Zenghao Duan, Fei Sun, Huawei Shen, and Xueqi Cheng. The evolution of thought: Tracking LLM overthinking via reasoning dynamics analysis. *arXiv preprint arXiv:2508.17627*, 2025. doi: 10.48550/arXiv.2508.17627. URL <https://arxiv.org/abs/2508.17627>.
- [13] Zhen Xiong, Yujun Cai, Zhecheng Li, and Yiwei Wang. Mapping the minds of LLMs: A graph-based analysis of reasoning LLMs. In *Proceedings of the 2025 Conference on Empirical Methods in Natural Language Processing*, pages 17751–17763, Suzhou, China, 2025. Association for Computational Linguistics. doi: 10.18653/v1/2025.emnlp-main.896. URL <https://aclanthology.org/2025.emnlp-main.896/>.
- [14] Shunyu Yao, Dian Yu, Jeffrey Zhao, Izhak Shafran, Thomas L. Griffiths, Yuan Cao, and Karthik R. Narasimhan. Tree of thoughts: Deliberate problem solving with large language models. In *Advances in Neural Information Processing Systems*, volume 36, pages 11809–11822. Curran Associates, Inc., 2023. URL <https://openreview.net/forum?id=5Xc1ecx01h>.

- [15] Yifan Zhang and Math-AI Team. American invitational mathematics examination (AIME) 2024. Hugging Face dataset, 2024. URL <https://huggingface.co/datasets/math-ai/aime24>.
- [16] Yifan Zhang and Math-AI Team. American invitational mathematics examination (AIME) 2025. Hugging Face dataset, 2025. URL <https://huggingface.co/datasets/math-ai/aime25>.
- [17] Tianjun Zhong, Linyang He, and Nima Mesgarani. From chains to DAGs: Probing the graph structure of reasoning in LLMs. *arXiv preprint arXiv:2601.17593*, 2026. doi: 10.48550/arXiv.2601.17593. URL <https://arxiv.org/abs/2601.17593>.
- [18] Zhanke Zhou, Zhaocheng Zhu, Xuan Li, Mikhail Galkin, Xiao Feng, Sanmi Koyejo, Jian Tang, and Bo Han. Landscape of thoughts: Visualizing the reasoning process of large language models. In *The Fourteenth International Conference on Learning Representations*, 2026. URL <https://openreview.net/forum?id=XpoQ812d0A>. Poster.

Appendix roadmap

- **Implementation and count conventions:** analysis subsets (§A.1); cache pipeline and graph hyperparameters (§A.2); block roles and bridge-vs-cycle convention (§A.3); reproducibility and statistics (§A.4).
- **Representation and family robustness:** block-scale and hyperparameter sensitivity (§B.1); representation ablation per pipeline×model (§B.2); fixed-scaffold split-half stability (§B.3); held-out atlas validation (§B.4); correct-run controlled isomer rate (§B.5); family-construction sensitivity (§B.6); isomer-discovery curves under run subsampling (§B.7).
- **Process-isomer geometry and dynamics:** reward-field construction (§C); multi-core / multi-family population summary (§C); per-model block-type localisation (§C.1); family-specific navigation diagnostics (§C.2); typed-state sensitivity and scope (§C.3); null-control ledger and label-permutation reward stress test (§C.4); family-TV null construction (§C.5); worked route report on GPQA-71 (§C.6).
- **Human annotation protocol:** family detection robustness (§D.1); annotation protocol (§D.2); Task A (BCC shared-state) (§D.3); Task B (process families) (§D.4); qualitative annotation cases (§D.5).
- **Cross-model replications:** Q2.5-72B cross-generation cross-scale (§E.1); Qwen3-32B within-family cross-scale (§E.2); Llama-8B cross-architecture (§E.3).

A Additional Experimental Details

A.1 Analysis Subsets and Count Conventions

Unique runs are sampled trajectories before graph construction; *analysed rows* are runs surviving slice selection. The second count is slightly smaller where individual runs yield no valid slice path.

Count ledger. The canonical primary atlas corpus has 318 unique benchmark problems evaluated under three primary models, giving $318 \times 3 = 954$ problem-model cells. At $N=64$ generations per cell this yields 61,056 sampled generations; after dropping 4 incomplete cache records, the corpus contains 61,052 runs. Graph-valid filtering further drops 430 runs whose stratified slice sampling yields an empty path, leaving 60,622 analysed rows. No largest-connected-component filter is applied: BCCs are computed component-wise on the selected graph, so disconnected rare routes are not silently removed. We reuse “954-cell corpus” as shorthand for these 954 problem-model cells. The reward-evaluable subset is stricter: after graph-valid filtering a cell must have at least 3 correct and 3 non-correct runs, at least two non-trivial blocks with non-empty run-block sequences, at least one seed-eligible block ($3 \leq n_b \leq n - 3$ visitors), and non-empty strictly positive support in $\mathbf{v}^{(24)}$. In the exported 479 reward-evaluable cells the minimum observed counts are 3 correct runs, 3 non-correct runs, 4 non-trivial blocks, 3 seed-eligible blocks, and one positive high-value-core block.

Table 4 Main analysis subsets used throughout the atlas version of the paper.

Analysis	Cells	Runs / rows	Notes
Canonical primary corpus	954	60,622 analysed rows	3 primary models, 5 non-code datasets, canonical <code>sep_up=8</code> , <code>k=6</code> , mutual- <code>kNN</code>
Reward-evaluable solution landscape	479 problem-model cells	cell-level subset	Requires ≥ 3 correct and ≥ 3 non-correct runs, ≥ 2 non-trivial blocks, at least one seed-eligible block, and non-empty positive field support
Core-eligible multi-family subset	403 problem-model cells	family-level kernels	Multi-family cells with at least one high-value core; used for family-TV and joint family/core checks; alignment readouts use natural denominators in Table 11
Cross-architecture replication	258	16,512 analysed rows	DeepSeek-R1-Distill-Llama-8B on AIME24, AIME25, and GPQA
Within-family cross-scale replication	318	20,352 analysed rows	Qwen3-32B (thinking mode) on the full 5-dataset non-code suite
Cross-generation cross-scale replication	318	20,196 analysed rows	Qwen2.5-Math-72B-Instruct on the full 5-dataset non-code suite
Process-family semantics (annotation)	8 cases	102 runs	46 within-family + 31 across-family judged pairs; two independent non-author annotators
BCC reasoning-state semantics (annotation)	36 cells	72 slice pairs	36 within-BCC + 36 matched across-BCC pairs; two independent non-author annotators

Derivation chain. The main atlas subsets form the strict refinement chain

$$954 \rightarrow 479 \rightarrow 403,$$

namely canonical corpus \rightarrow reward-evaluable cells \rightarrow core-eligible multi-family cells. The alignment readouts in Table 11 then use natural denominators: for example, specialization is averaged on the 324 multi-core reward-evaluable cells, while family-TV uses the 403-cell subset.

A.2 Activation-Cache and Graph Implementation

Sparse activation logging. We record post-gating MLP intermediates under the standard SwiGLU/GeGLU convention used by Qwen3, DeepSeek-R1-Distill-Qwen, DeepSeek-R1-Distill-Llama, and Qwen2.5-Math. Let $u_{\ell,t}, g_{\ell,t} \in \mathbb{R}^{d_{\text{ff}}}$ denote the FFN “up” and “gate” pre-activations at layer ℓ and token t , and let $\phi(\cdot)$ denote the gating nonlinearity (SiLU here). We score each neuron by the positive part of its post-gating contribution,

$$h_{\ell,t} \triangleq \phi(g_{\ell,t}) \odot u_{\ell,t}, \quad a_{k,t} \triangleq \max(0, (h_{\ell,t})_j), \quad (7)$$

with each neuron keyed across layers as

$$k = (\ell \ll 16) \mid j. \quad (8)$$

At each token we retain the top `global_topk=2000` neurons by $a_{k,t}$.

Window aggregation and slice keys. Tokens are grouped into rows of `slice_size=32`. For row r with token-index set T_r , we form $A_{k,r} = \sum_{t \in T_r} a_{k,t}$ and keep the `slice_topk=500` neurons with largest mass:

$$\mathcal{K}_r = \text{top}_{K=500}\{k : A_{k,r}\}, \quad |\mathcal{K}_r| \leq K. \quad (9)$$

The analysis pipeline then aggregates every consecutive `sep_up=8` rows into one analysed slice, so one analysed slice summarises 256 tokens of CoT.

Graph construction. Canonical SliceGraph construction uses mutual-`kNN` with `k=6`, distance scale $\sigma=0.35$, and size cap $M=2,600$ slices per problem. Problems exceeding M are stratified-sampled over runs and

positions before graph construction. Edge weights are RBF transforms of Jaccard distance on the sparse key sets.

A.3 Block Roles, Thresholds, and Bridge-vs-Cycle Convention

The five block roles used in §3.2 are assigned from each block’s run coverage c_b , size $|b|$, dominant-answer purity π_b , unique run count $n_{\text{runs}}(b)$, and median position $\text{medpos}(b)$:

$$\text{role}(b) = \begin{cases} \text{SHARED_TRUNK} & c_b > 0.4, |b| \geq 6, \text{medpos}(b) \leq q_{0.5}^{\text{trunk}} \\ \text{ANSWER_BASIN} & |b| \geq 6, \text{medpos}(b) > q_{0.5}^{\text{basin}}, \pi_b \geq 0.6, n_{\text{runs}}(b) \geq 3 \\ \text{WEAK_BASIN} & |b| \geq 6, \text{medpos}(b) > q_{0.5}^{\text{basin}} \text{ but answer-basin criteria fail} \\ \text{DECISION_POINT} & |b| \leq 5 \text{ and touches an articulation point} \\ \text{INTERMEDIATE} & \text{otherwise.} \end{cases} \quad (10)$$

Bridge-vs-cycle convention. The biconnected decomposition partitions the graph into trivial K_2 bridge blocks and non-trivial blocks of size $|b| \geq 3$ that are 2-vertex-connected. All main-text constructs operate on the non-trivial subset because including bridges inflates length-driven fragmentation while adding little semantic content to the atlas.

Primary-block tie breaks. When a slice is covered by multiple non-trivial blocks, the primary block $b_{r,t}^*$ is chosen by largest block size in nodes, with ties broken by larger unique-run count, earlier minimum slice position, then smaller block id. Slices with no non-trivial block are skipped in typed-state trajectories rather than mapped to a sentinel.

A.4 Reproducibility and Statistics

Fresh CoT generation uses framework-level nondeterminism rather than fixed per-run sampling seeds, so bitwise reruns of the analysis are supported by the generated cache and graph summaries; the paper and code repository provide full algorithmic details and exported headline tables. The paper reports problem-clustered bootstrap intervals ($B=1000$) for headline proportions and means where appropriate, and null-controlled z-scores for graph or transition-structure diagnostics. Multiple related null-based tests within the same experiment family use Benjamini–Hochberg FDR control.

Model checkpoints. All measured systems are open-weight Hugging Face checkpoints (Table 5); no fine-tuning is applied and all generations are zero-shot CoT with each model’s default chat template.

Table 5 Model checkpoints used for CoT generation.

Paper name	HuggingFace ID	Mode / setting	Arch.
R1-8B	deepseek-ai/DeepSeek-R1-0528-Qwen3-8B	thinking-only	Qwen3
Think	Qwen/Qwen3-4B-Thinking-2507	thinking-only	Qwen3
Inst	Qwen/Qwen3-4B-Instruct-2507	non-thinking-only	Qwen3
Llama-8B	deepseek-ai/DeepSeek-R1-Distill-Llama-8B	thinking-only	Llama-3.1
Qwen3-32B	Qwen/Qwen3-32B	enable_thinking=True	Qwen3
Q2.5-72B	Qwen/Qwen2.5-Math-72B-Instruct	default	Qwen2.5

Hardware and compute. CoT generation: 8× NVIDIA H20-96GB GPUs, using flash-attention-2; the 72B model was served with 8-way tensor parallelism, smaller models on a single H20. Estimated total generation cost: ~200 GPU-hours across all models and benchmarks. Activation-cache extraction ran on the same hardware during generation. The SliceGraph analysis pipeline (graph construction, BCC decomposition, reward field, and typed-state diagnostics) runs entirely on CPU and completes in 2–5 s per problem at $N=64$ runs.

Table 6 CoT generation protocol. We intentionally use a uniform sampling protocol across all measured models for atlas comparability, rather than each model card’s recommended decoding parameters; model-specific chat templates and mode switches are still respected.

N per problem-model cell	64
Temperature	0.7
Top- p	0.9; uniform across all models
Top- k	disabled
max_tokens	32,768
Chat template	each model’s default chat template applied via <code>tokenizer.apply_chat_template</code> ; no system prompt
User prompt (math)	Return your final response within <code>\boxed{}</code> . Question: <code>\n{problem}</code>
User prompt (GPQA)	Please answer the following multiple choice question: Question: <code>{question}</code> Options: A. <code>{A}</code> B. <code>{B}</code> C. <code>{C}</code> D. <code>{D}</code> Return your final response within <code>\boxed{}</code> and only include the letter choice (A, B, C, or D) as your final response.
Answer extraction	parse last <code>\boxed{...}</code> via brace-matched extraction; numeric benchmarks verified with <code>math_verify</code> (symbolic equivalence); GPQA verified by exact single-letter match
Sampling randomness	framework-level nondeterminism; analysis reruns use distributed caches
Mean / median output tokens	10,208 / 7,578
Length-truncated runs	4,210/61,052 = 6.9% (primary corpus; retained, counted as non-correct if no answer extracted)

Software versions. Python 3.12; PyTorch 2.6; Transformers 5.3; NetworkX 3.6 (BCC decomposition via `biconnected_components`, Louvain via `louvain_communities`); NumPy 2.2; SciPy 1.17; scikit-learn 1.8 (PCA ablation); `sentence-transformers` (MiniLM ablation).

Random seeds. Louvain community detection uses seed 42; problem-clustered bootstrap uses $B=1,000$ resamples with `numpy.random.seed(0)` per bootstrap call; graph-null rewiring uses 3 independent seeds per variant. Temperature-sampled CoT runs have no fixed seed (each run is an independent sample from the model’s output distribution).

B Representation and Family Robustness

B.1 Block-Scale Sensitivity and Hyperparameters

The paper uses the graph-theoretic split between trivial BCCs (K_2 , bridges) and non-trivial biconnected blocks ($|b| \geq 3$), i.e. 2-vertex-connected cyclic regions. Moving from the full decomposition ($m=2$) to the non-trivial convention ($m=3$) changes the object substantially: the mean retained block count drops from 575.2 to 49.5. Even so, the family-level atlas picture is stable. Including bridges shifts the multi-family headline only slightly (85.5% \rightarrow 86.8%) but overfragments the partition, raising mean correct-only families per cell from 4.66 to 11.27 and the between-family length-variance ratio from 0.460 to 0.697. We therefore retain bridges as connectors but not as semantic regions.

Across a 30-configuration sweep over (`sep_up`, k , `mutual`) the default configuration is not a narrow optimum, and the multi-family rate of §4.4 remains stable across all sampled settings. On run-number sufficiency, $N=64$ retains 95.0% of the process-family coverage observed on deeper $N=256$ caches.

RBF kernel scale σ . The edge-weight scale $\sigma \in \{0.20, 0.35, 0.50\}$ has no effect on topology-dependent readouts because the mutual- k NN construction determines graph topology independent of weight scaling: σ modulates edge strength but not edge existence. On the sweep-eligible subset, the multi-family rate remains 97.8% and the pairwise isomer rate remains 76.6% at all three values.

Reward-field diffusion α and core quartile q . Varying the PageRank damping $\alpha \in \{0.50, 0.65, 0.80\}$ and core extraction percentile $q \in \{0.50, 0.75, 0.90\}$ preserves the correct-run field advantage in all configurations: non-canonical variants produce equal or larger correct-vs-incorrect separation on field-score and entry-progress

metrics across all three models. The canonical $\alpha=0.65$, $q=0.75$ is therefore a *conservative* choice; no variant degrades the reward-field signal or inverts the multi-core structure.

Role thresholds. An OAT sweep over 8 role parameters (46 configurations including default) shows sign stability for the headline family-TV-above-null direction across all 19 non-degenerate configurations. Family-TV does not affect family construction, which uses block co-visitation. The typed-state Family-TV diagnostic does use role labels, but the OAT sweep shows its sign and qualitative conclusions are stable under all non-degenerate role-threshold variants.

B.2 Representation Ablation: Per-(Pipeline×Model)

The full representation ablation discussed in §4.3 is reported here. Pipelines are mutual- k NN graphs with the same BCC decomposition and vary only the slice representation: cosine on the same activation keys; PCA-cosine at $d \in \{2, 10, 50\}$; and all-MiniLM-L6-v2 sentence embeddings on 256-token slice text. “collapsed” indicates a graph too degenerate for a useful BCC decomposition. We interpret the MiniLM failure as a same-problem saturation effect: within one problem, slice text embeddings preserve topical relatedness but compress many slices into a narrow similarity range, leaving too little within-problem variance for mutual- k NN to separate local trunks, forks, and re-joins.

Table 7 Representation ablation, full per-(pipeline×model) family geometry breakdown: multi-fam % / mean correct families per cell on the same graphs as Table 1 of the main text.

Pipeline	R1-8B	Think	Inst
Jaccard kNN (ours)	89.3/5.14	86.2/4.61	81.1/4.21
Cosine kNN	88.1/4.80	85.5/4.36	79.6/3.87
Overlap kNN	87.7/4.77	85.5/4.36	79.6/3.87
PCA-50 + cos	81.4/3.38	81.4/3.33	73.8/3.00
PCA-10 + cos	84.9/3.45	81.6/3.40	73.5/2.96
PCA-2 + cos	83.3/3.65	82.1/3.76	74.1/3.52
MiniLM slice	<i>collapsed (n=5)</i>	<i>collapsed (n=5)</i>	<i>collapsed (n=11)</i>

B.3 Fixed-Scaffold Split-Half Stability

As a lightweight held-out-style check, we split each cell’s runs into two deterministic 32/32 halves after constructing the canonical SliceGraph and non-trivial block scaffold. Within each half we induce the run-level co-visitation graph on normalized-correct runs only and rerun the same Louvain family detector. This does not yet prove that a graph built from one half can project every held-out run into a matched family, but it tests whether the observed family multiplicity depends on a small set of runs that vanish under resampling.

Across 779 non-code primary cells with at least two correct runs in both halves, both halves are multi-family in 97.2% of cells (problem-clustered bootstrap 95% CI [96.0, 98.2]%). The full-cell multi-family rate on this split-valid subset is 99.7%. The mean absolute difference in half-level family count is 1.12 families (median 1), and the two half-level pairwise family-isomer rates are 75.1% and 75.7%, with median absolute pair-rate difference 5.1 points.

We treat this as a lightweight stability check. The stricter held-out validation below completes the picture.

B.4 Held-Out Atlas Validation

To move beyond a fixed-scaffold stability check, we perform a fully held-out validation: (i) build a SliceGraph from a random 32-run *train half*; (ii) for each held-out slice, compute nearest neighbours against train-half slices only using its sparse activation keys (without test-test edges or the full 64-run graph topology) and assign it to that neighbour’s primary non-trivial block; (iii) compute covisitation families on the held-out correct runs using the train-half block scaffold; and (iv) measure whether the held-out partition is multi-family and how it relates to the full-sample partition.

We run $R=5$ random splits per cell across 834 canonical primary cells with ≥ 4 correct runs. Block coverage from test onto train blocks is **95.5%**, confirming that the scaffold generalizes. Held-out cells are multi-family in **91.0%** of cases (vs. 97.8% on the full 64-run sample), with mean held-out pairwise isomer rate **60.1%** (vs. 77.8% full-sample). NMI between full-sample and held-out family labels is moderate (0.24 median), indicating that exact family identities are not stable under a half-sample scaffold. We therefore use this held-out check to support multi-family presence and block coverage, not one-to-one family recovery.

B.5 Correct-Run Controlled Isomer Rate

Family count might be confounded by the number of correct runs: cells with higher accuracy have more correct runs and might discover more families simply due to sample size. We control for this by fixing the number of correct runs to $m \in \{4, 8, 16\}$, subsampling m correct runs per cell (with $R=10$ replicates) and recomputing the pairwise isomer rate on the same block scaffold.

Table 8 Pairwise isomer rate at fixed correct-run count m . Mean over $R=10$ replicates per cell, pooled across three primary models. Multi-family structure persists even at $m=4$.

	$m=4$	$m=8$	$m=16$
Mean isomer rate	58.2%	69.6%	75.2%
Multi-family %	82.1%	99.7%	100%
Mean families	2.3	3.3	4.4

Even at $m=4$, the multi-family rate is 82.1% and the pairwise isomer rate is 58.2%, still substantial. At $m=8$ the rate already recovers to $\sim 70\%$, and at $m=16$ it nearly matches the full-sample 76.6% headline. The claim is therefore not an artefact of high correct-run counts inflating opportunity.

B.6 Family Construction Sensitivity

We sweep the two main Louvain hyperparameters—resolution $\rho \in \{0.5, 1.0, 1.5, 2.0\}$ and weighted-Jaccard edge threshold $\tau \in \{0.025, 0.05, 0.1\}$ —across 834 primary cells.

Table 9 Pairwise isomer rate (full-cell block weights) under a resolution \times threshold sweep on the correct-only covisitation graph. Canonical configuration: $\rho=1.0, \tau=0.05$.

Resolution	$\tau=0.025$	$\tau=0.05$	$\tau=0.1$
0.5	0.247	0.365	0.552
1.0	0.744	0.766	0.793
1.5	0.857	0.865	0.868
2.0	0.917	0.915	0.913

At $\rho=1.0$ the isomer rate is stable across thresholds (74–79%), and the multi-family rate exceeds 96% for all three threshold values. Lower resolution ($\rho=0.5$) under-partitions and higher resolution ($\rho \geq 1.5$) over-partitions, but the multi-family presence is robust across $\rho \geq 1.0$. Replacing full-cell block coverage weights with correct-only weights changes the canonical isomer rate by only 3.4 percentage points (76.6% \rightarrow 73.2%), confirming that incorrect runs’ contribution to rare-block upweighting is not the driver.

B.7 Isomer-Discovery Curves under Run Subsampling

We subsample the existing $N=64$ caches at $N \in \{8, 16, 32, 64\}$ ($R=5$ replicates, uniform without replacement) and recompute family detection and core masks at canonical hyperparameters.

C Process-Isomer Geometry and Dynamics

The reward field is used in this paper only as a *label-seeded explanatory solution landscape*. A cell enters the reward-evaluable subset only when the leave-one-out seed is stable enough to define such a landscape; this is

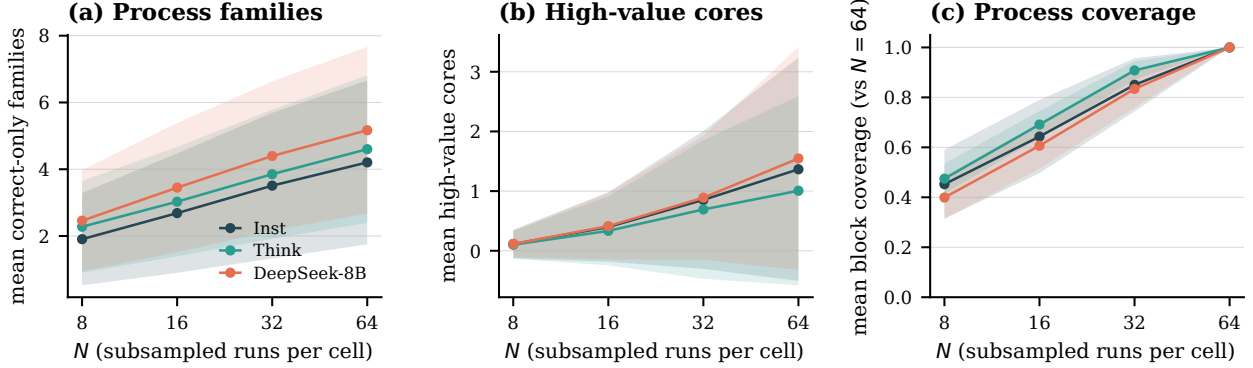


Figure 6 Isomer-discovery curves under run subsampling. (a) Correct-only family count, (b) high-value-core components, (c) block coverage relative to $N=64$. Block coverage saturates around $N \approx 32$; family and core counts keep growing as rare-block neighbourhoods enter the sample.

Table 10 Full model \times dataset route multiplicity including replication models. Entries: % cells with ≥ 2 correct-only families / mean correct families. Top: primary corpus; bottom: replication models. Llama-8B covers AIME24, AIME25, and GPQA only.

Model	AIME24	AIME25	BRUMO25	GPQA	HMMT25	All
R1-8B	86.7 / 4.87	86.7 / 4.80	86.7 / 4.57	92.4 / 5.50	76.7 / 3.97	89.3 / 5.14
Think	93.3 / 5.07	86.7 / 5.10	96.7 / 4.77	85.9 / 4.60	70.0 / 3.57	86.2 / 4.61
Inst	83.3 / 4.20	70.0 / 3.43	76.7 / 3.70	87.9 / 4.72	50.0 / 2.17	81.1 / 4.21
Llama-8B	76.7 / 4.80	53.3 / 3.10		82.3 / 3.98		78.3 / 3.98
Qwen3-32B	93.3 / 5.17	90.0 / 4.93	96.7 / 4.80	88.4 / 4.56	86.7 / 4.17	89.6 / 4.64
Q2.5-72B	46.7 / 1.93	36.7 / 1.33	46.7 / 2.40	86.4 / 4.18	13.3 / 0.47	67.3 / 3.18

a construction requirement, not a classification objective.

Reward-field propagation details. For a cell with n graph-valid runs and block visitor set \mathcal{R}_b , the global seed used for high-value cores is

$$v_b^{(0)} = \mathbf{1}[3 \leq n_b \leq n - 3] \left(\frac{1}{n_b} \sum_{r \in \mathcal{R}_b} y_r - \frac{1}{n} \sum_r y_r \right) \left(\frac{n_b}{n} \right)^{1/2}, \quad n_b = |\mathcal{R}_b|. \quad (11)$$

The run-level leave-one-out variant used for per-run overlays removes that run from both the block and cell denominators. The diffusion graph has non-trivial blocks as nodes; K_2 bridges are not diffusion nodes. Let E_{BC} connect two non-trivial blocks that share an articulation point in the block-cut tree, and let E_{temp} connect consecutive distinct primary blocks in a compacted run path. Temporal edges are symmetrized, multiplicities are binarized, and the raw adjacency is

$$A_{ij}^{raw} = \mathbf{1}[i = j] + \mathbf{1}[(i, j) \in E_{BC} \cup E_{temp}], \quad P_{ij} = \frac{A_{ij}^{raw}}{\sum_k A_{ik}^{raw}}. \quad (12)$$

Thus block-cut and temporal edges have equal weight ($\lambda = 1$) after binarization, and the self-loop weight is 1. In all experiments we use $\alpha=0.65$ for 24 steps,

$$\mathbf{v}^{(t+1)} = \alpha \mathbf{v}^{(0)} + (1-\alpha) \mathbf{P}\mathbf{v}^{(t)}. \quad (13)$$

We keep $\mathbf{v}^{(24)}$ as the field used throughout §4.5; the high-value core is the top quartile of its strictly positive support. After 24 iterations, each propagated field—pooled or family-conditioned—is independently rescaled

by its own ℓ_∞ norm. Core masks, connected components, and specialization statistics are invariant to positive rescaling; field-sharpness ratios (Equation 15) should be read under this per-field normalization convention.

Alignment and non-redundancy definitions. For a cell with high-value-core components C_1, \dots, C_K and a correct-only family f , let B_f be the union of non-trivial blocks visited by runs in f and $m_f(k) = |B_f \cap C_k|/|C_k|$. For $K \geq 2$ we normalize each non-zero row to $p_f(k) = m_f(k)/\sum_j m_f(j)$ and define

$$\text{Spec} = 1 - \frac{1}{|F_+|} \sum_{f \in F_+} \frac{H(p_f)}{\log K}, \quad (14)$$

where F_+ are families with non-zero core footprint. The reported 0.59 is averaged on the 324 multi-core reward-evaluable cells. For a family-conditioned field \mathbf{v}_f , computed by setting correctness labels outside family f to zero before applying Equations 11–13, field sharpness is

$$\text{Sharp}(f) = \frac{\max_i v_{f,i}^{(24)}}{\max_i v_i^{(24)}}. \quad (15)$$

Coverage loss uses the most coverage-critical family in a cell:

$$\Delta_{\max} = \max_f \frac{|(\cup_g B_g) \setminus (\cup_{g \neq f} B_g)|}{|\cup_g B_g|}. \quad (16)$$

The 94.5% headline is $\Pr(\Delta_{\max} > 0.10)$ over the 816 canonical cells with at least two correct-only families.

Table 11 Multi-modal reward geometry (non-code). Sections A–C use the three primary models; section D adds the Llama cross-architecture replication.

Statistic	Value
<i>A. High-value core disconnectedness (n=479)</i>	
% cells with ≥ 2 core components	67.6%
Mean / median # core components	2.61/2
Size ratio: 2nd / 1st component	0.54
<i>B. Correct-only families (n=954)</i>	
% cells with > 1 correct family	85.5%
Mean correct families / cell	4.66
Pairwise family-isomer rate (n=834 cells)	mean 76.6%, median 79.6%
Problem-clustered bootstrap CI for mean	[75.6, 77.5]%
Split-half both-halves multi-family (n=779 cells)	97.2%
Length-variance ratio	0.460
Modularity null z (median)	35.54
<i>C. Alignment and non-redundancy (natural denominators)</i>	
Family-core footprint specialization (multi-core cells, n=324)	0.59
Family field-max / pooled-global field-max (2,094 family fields)	1.55x
Jaccard(family core, global core)	0.17
Spearman(#components, #families)	0.08
% multi-family cells where most critical family removal loses $> 10\%$	94.5%
Core-divergence increment over family-isomer rate	+1.3 pp
<i>D. Llama cross-architecture replication</i>	
% with ≥ 2 core components (n=194)	78.4%
% with > 1 correct family (n=258)	78.3%
Family-core footprint specialization (multi-core)	0.60
Family field-max / pooled-global field-max	1.46x
Length-variance ratio	0.469

The pairwise family-isomer rate is the primary Definition 1 rate: it is computed within each problem-model cell that has at least two normalized-correct runs, as the share of unordered correct-run pairs assigned to

different correct-only process families, then averaged across cells. Core divergence is reported separately as a value-landscape refinement (§4.5).

C.1 Per-Model Block-Type Localisation

The pooled reward-field statistics collapse a model-dependent block-type localisation that is itself informative. Inst concentrates at SHARED_TRUNK; R1-8B, Think, and Llama-8B concentrate at ANSWER_BASIN. All four therefore exhibit a localized high-value landscape; they differ only in which structural niche hosts it.

Table 12 Per-model mean propagated reward field by block-type role on the canonical reward-field corpus. Bold cells indicate the dominant block-type per model.

Model	shared_trunk	answer_basin	weak_basin	intermediate	decision_point
Inst	0.138	0.001	0.016	0.005	0.003
R1-8B	0.062	0.252	0.062	0.029	0.023
Think	0.064	0.236	0.046	0.030	0.023
Llama-8B	0.031	0.123	0.044	0.006	0.006

C.2 Family-Specific Navigation Diagnostics

The typed-state transition model is used to compare how different correct-only families traverse the same atlas. The population-level dynamics headline in the atlas version is family-specific kernel divergence rather than an auxiliary task objective.

For each run we map the primary non-trivial block at slice t to $z_{r,t} = (\text{role}(b_{r,t}^*), \text{posbin}(\tau_t), \text{core}(b_{r,t}^*))$, compact consecutive duplicates, and append absorbing correct/wrong terminals. Transition counts C are Laplace-smoothed into

$$P_{ij} = \frac{C_{ij} + \alpha_{\text{smooth}}}{\sum_{j'} C_{ij'} + \alpha_{\text{smooth}} |\mathcal{S}|}, \quad \alpha_{\text{smooth}} = 0.5. \quad (17)$$

Family-TV averages row-wise kernel divergence,

$$\text{TV}(P_f, P_{f'}) = \frac{1}{2|\mathcal{S}|} \sum_{i \in \mathcal{S}} \|P_f(i, \cdot) - P_{f'}(i, \cdot)\|_1. \quad (18)$$

In the released implementation, the averaging set \mathcal{S} includes the two absorbing terminal rows (EOS_{correct}, EOS_{wrong}); because both are forced absorbing with identical rows across families, they contribute zero TV. Removing them rescales the denominator but does not affect the matched-null comparison reported in §4.6. The pooled-kernel committor solves $(I - Q)q = r_A$, where Q is the transient-to-transient block and r_A is the transition vector into EOS_{correct}. The three-step escape hazard is $h_3 = \sum_{i \in \mathcal{C}} \hat{\pi}(i) \sum_{j \notin \mathcal{C}} P_{ij}^3$; return and MFPT readouts use the same smoothed kernel and are retained as case-level diagnostics.

Table 13 Family-specific navigation diagnostics on the core-eligible multi-family subset ($n=403$).

Statistic	Value
Median family pairwise kernel TV	0.137
% cells with real TV > null p_{95}	80.9%
Median null z	3.14
Corr.(family-TV, static specialization)	-0.07

The pooled-kernel committor, MFPT to core, escape hazard, and post-escape return remain useful *case-level atlas readouts* for understanding how one family navigates relative to another. In this atlas version they are not treated as standalone population claims.

Table 14 Common-support family-TV diagnostic. TV is averaged only over typed-state rows visited by both families in a pair; the null shuffles run-to-family assignments while preserving family sizes.

Statistic	Value
Eligible cells	403
Median common-support family TV	0.206
Median common-support null p_{95}	0.183
% cells with common-support TV > null p_{95}	77.4%
Median common-support null z	3.45
Median shared typed states per family pair	7.0

C.3 Typed-State Sensitivity and Scope

Family-TV is the only population-level dynamics statistic we headline, because it is the most stable to mild changes in smoothing and role thresholds. The companion pooled committor, MFPT, escape, and return diagnostics remain informative for inspecting one fixed atlas, but their absolute numeric values are more sensitive to role-threshold choices and sparse-transition smoothing. We therefore use them as descriptive overlays on the process atlas rather than as independent paper claims.

C.4 Null-Control Ledger

Table 15 maps each main-text claim to the corresponding weak reading and diagnostic used to control it.

Table 15 Claim-to-control ledger for the main atlas readouts.

Claim	Weak reading	Control / diagnostic
Families are route units	arbitrary graph clusters	human strategy audit, modularity null
Process isomers are common	few-run sampling artifact	pairwise rate, split-half stability
High-value cores are multi-basin	heatmap fragmentation	core-size ratio, label-permutation caveat
Family dynamics differ	support mismatch only	family-label null, common-support TV

The paper uses several nulls, each aimed at a different possible artifact. We use five null families, each targeting a different possible confound:

1. **Degree-preserving graph rewire** — preserves the degree sequence but destroys local adjacency; used for the family modularity headline (median $z=35.54$).
2. **Block-type-preserving rewire** — preserves role counts and type marginals; used as a structural-sensitivity stress test (effect-drop only).
3. **Family-label shuffle** — preserves family sizes and typed-state support but destroys route-specific labels; the exported population null for family-TV (80.9% above p_{95} , median $z=3.14$).
4. **Temporal-order shuffle** — preserves visited typed states but destroys transition order; used for kernel, escape, return, and MFPT stress tests (effect-drop only).
5. **Label permutation** — preserves graph topology, family partition, and per-cell label count but randomises correctness association; the reward-core stress test (Table 16).

Items 1 and 3 generate the exported headline nulls; items 2 and 4 are validity-ladder stress tests and should not be read as independent population claims.

Label permutations tend to scatter positive seed mass, which can create more disconnected random cores and higher apparent specialization than the real labels. We therefore do not use this stress test as a one-sided null for multi-core counts. Its main diagnostic value is that real family-conditioned cores overlap the real global core far more than permuted labels do, while field sharpness alone is comparable to the permutation range and is interpreted only together with the family/core geometry above.

Table 16 Label-permutation reward-field stress test. Permutations preserve the graph topology, family partition, and the number of correct labels in each reward-evaluable cell, but randomize which runs are correct. The permutation range reports shuffle-level p_5 - p_{95} across 100 shuffles.

Readout	Real	Label-perm. mean [p_5, p_{95}]	z
Multi-core rate	67.6%	85.4% [83.3,88.1]%	-11.44
Family-core footprint specialization, real multi-core cells	0.59	0.74 [0.72,0.76]	-11.87
Family field-max / pooled-global field-max, field-weighted	1.55×	1.55× [1.48,1.70]	0.08
Jaccard(family core, global core), field-weighted	0.17	0.10 [0.097,0.105]	29.36

C.5 Family-TV Null Construction

For each core-eligible multi-family cell, the family-TV null keeps family sizes and typed-state support fixed while shuffling family labels across trajectories before re-estimating per-family kernels. This preserves the atlas and its coarse traffic levels while erasing route-specific navigation structure. The main-text 80.9%-above-null and median- $z=3.14$ headline is measured against this null.

Common-support TV. A stricter diagnostic averages TV only over typed states visited by both families in a pair. This tests whether families move differently even where they share support, rather than only because they visit different states. Table 14 reports the matched family-size shuffle null and the shared-support denominator summary.

C.6 Worked Route Report on GPQA-71

As a worked example we pick GPQA-71 under **Inst** (Qwen3-4B-Instruct-2507): seven correct-only process families covering 38 non-trivial blocks across four disconnected high-value-core components. Removing the single most coverage-critical family loses 55.3% of total block coverage, and the loss-if-removed shares sum to 92.1%, confirming that route coverage is family-unique rather than redundantly shared. The four core components are occupied by different families (F6→core 0, F0→core 1, F2/F5→core 2/3), while F1, F3, F4 are off-core under the top-quartile mask. Per-family coverage plots and the full summary card are included in the code repository.

D Annotation Protocols and Family Robustness

This section covers family-detection robustness and the two human-annotation tasks used in §4.2. Task A audits BCC shared-state semantics; Task B audits process-family same-strategy semantics.

Table 17 Compact summary of annotation and family-validation statistics, split by task. Top block: Task B (process families); bottom block: Task A (BCC shared-state).

Statistic	Value
<i>Task B (process families)</i>	
Within-family decisive agreement (Annotator A)	94.4%
Self-consistency κ (Annotator A)	0.65
Across-family cross-annotator κ ($A \times B$)	0.737
Decisive exact agreement, family pack ($A \times B$, $n=55$)	81.8%
<i>Task A (BCC shared-state)</i>	
BCC agreement vs. ground-truth (Annotator B, $n=72$)	90.3%
BCC agreement vs. ground-truth (Annotator A, $n=72$)	88.9%
BCC-pack cross-annotator κ ($A \times B$, decisive $n=71$)	0.97
Matched non-articulation specificity (Annotator B)	36/36

D.1 Family Detection Robustness

The default 85.5% multi-family rate is not Louvain-specific: greedy modularity reproduces the same direction and magnitude, while a degree-preserving modularity null is decisively weaker (median $z=35.54$). Label propagation is included only for transparency and is not preferred because it collapses weighted-Jaccard family graphs pathologically.

D.2 Annotation Protocol

Annotators A and B are two non-author external annotators with mathematical reasoning and LLM-trace experience. They are blind both to the project hypothesis and to within/across pair labels, and cross-label both the BCC pack (Task A) and the process-family pack (Task B) under matched strict rubrics.

Pair construction. Task A (BCC): for each BCC block, a within-BCC pair is formed by selecting two runs from different trajectories with the smallest positional gap; a matched across-BCC control with the same correctness label and the smallest absolute position offset is paired. For articulation transitions, the first positive articulation-boundary crossing per trajectory is matched with a phase-matched non-articulation control. Task B (families): 8 cases are selected across 3 models and 3 datasets, each with ≥ 4 correct-only families and ≥ 5 decision forks; 2 runs per family are sampled from normalized-correct runs only, balanced by length and model/dataset via stratified sampling, yielding 46 within-family + 31 across-family pairs from 102 runs.

Blinding and randomisation. The self-consistency re-review uses a strictly blinded prompt template that hides: (i) within-vs-across family labels, (ii) original first-pass judgements, (iii) family IDs. Pair order is randomised. Pair identity is tracked by a deterministic 12-character hash of (case_id, sorted run IDs). The cross-annotator wave uses the same blinded pack in the same randomised order, in an independent session with no access to the primary annotator’s responses.

Response schemas. Task A: `annot_same_reasoning_state` \in {yes, no, uncertain}, `annot_confidence` \in 1–5, plus free-text `annot_notes`. Task B: `same_strategy` \in {yes, no, uncertain}, `confidence` \in 1–5, `justification` (one sentence).

Uncertainty handling. All tasks use a three-value scheme (yes/no/uncertain). The instruction states: “Use `uncertain` sparingly—only when two runs share a framework but execute it in materially different ways.” We report two denominators: *raw* (uncertain counts as negative) and *decisive* (uncertain excluded from both numerator and denominator). The decisive rate is the primary claim metric; raw counts or uncertain counts are reported where they affect interpretation.

Cohen’s κ calculation. We use unweighted Cohen’s κ with the label set {yes, no, uncertain}. For the across-family sub-task, labels are inverted (`different_strategy=yes` \rightarrow `same_strategy=no`) before computing κ . Key values: Annotator A self-consistency $\kappa=0.65$ (overall, 76 decisive), across-family-only $\kappa=0.80$; cross-annotator across-family $\kappa=0.737$ (30 decisive pairs).

D.3 Task A: BCC Shared-State Audit

Protocol. The core BCC pack contains 72 slice-text pairs: 36 within-BCC pairs and 36 length-matched across-BCC controls. Both annotators judge whether the two slices represent the same reasoning state. Separately, we construct an articulation transition pack of 72 adjacent-slice comparisons (36 true articulation crossings and 36 matched non-articulation controls); this auxiliary pack is used as a precision-side control rather than as a second headline task.

Cross-annotator BCC agreement. On the 72-pair BCC slice-text pack, Annotator B agrees with the BCC-derived labels on **90.3%** of pairs and Annotator A reaches 88.9%. Direct A-vs.-B agreement is **97.2%** on all decisive comparisons ($\kappa=0.97$, $n=71$), with only two decisive disagreements. This is the strongest evidence that the BCC/shared-state interpretation is independently recoverable.

D.4 Task B: Process-Family Same-Strategy Audit

Protocol. We select 8 cases across the 3 primary models and three datasets (AIME24, HMMT25, and GPQA), requiring at least 4 correct-only families, at least 5 decision forks, and problem accuracy between 40–80%. From these cases we sample 102 runs, yielding a final judged pack of 77 blinded run pairs: 46 within-family and 31 across-family. Input CoTs are truncated to 15,000 characters via a front/middle/tail (5k/5k/5k) scheme with omissions marked explicitly.

Cross-annotator family agreement. The numbers referenced in the main text are: (i) Annotator A’s within-family decisive agreement rate of 94.4% (34/36 decisive pairs judged same-strategy); (ii) cross-annotator $\kappa=0.737$ on the across-family slice ($n=30$ decisive pairs, raw agreement 90.0%); and (iii) 81.8% exact agreement on the subset where both annotators give a decisive judgement ($n=55$).

Across-family differentiation rate. Of 31 across-family pairs, Annotator A gives 10 decisive “different strategy” judgements, 11 decisive “same strategy,” and 10 uncertain. The decisive differentiation rate is therefore $10/21=47.6\%$. This partial separation is expected: SliceGraph families are defined by co-visitation of non-trivial blocks (a sub-token-level structural signal), which captures finer process differences than a human annotator’s coarse “same strategy?” rubric. Under a matched strict rubric, Annotator B’s family-level yes-rate is within 4 pp of Annotator A’s, so the family claim is not a single-annotator artifact.

D.5 Qualitative Annotation Cases

Table 18 summarises four representative cases used for qualitative inspection; full anonymised verbatim excerpts are included in the code repository as `annotation_cases/`.

Table 18 Qualitative annotation cases. Confidence is on a 1–5 scale.

Case	Task	Judgement	Conf.	Diagnostic point
A1	BCC within/across	same vs. different state	4/5	Answer-finalisation pair vs. quadratic-solving control (AIME24)
A2	Articulation transition	strategy shift	5/5	Divisor enumeration \rightarrow prime-factorisation pivot (HMMT25)
B1	Within-family	same strategy	5/5	Both runs set up binary-expansion identity identically (HMMT25)
B2	Across-family	process-isomer pair	5/5	Numerical-first vs. theory-first route to same answer (HMMT25)

E Cross-Model Replications

E.1 Cross-Scale Replication on Qwen2.5-Math-72B-Instruct

We replicate the full canonical pipeline—including the reward field, multi-core decomposition, family-core specialization, and family-TV—on Qwen2.5-Math-72B-Instruct (20,352 sampled runs, 20,196 graph-valid rows; 318 non-code problems on AIME24/25, BRUMO25, GPQA, HMMT25) under the identical configuration (`sep_up=8`, `k=6`, `mutual-kNN`, $\sigma=0.35$, $M=2,600$; reward $\alpha=0.65$, `core_q=0.75`).

Process-family heterogeneity. Under canonical Louvain, 72B retains multi-family structure but attenuates on saturated math datasets where many problems are solved near-deterministically. On GPQA, where the model is less saturated, the multi-correct-family rate is **86.4%**, essentially matching the 3-model 85.5% headline.

Reward-field and multi-core structure. The multi-core rate drops to 42.9% (vs. 67.6% primary), consistent with 72B solving many problems near-deterministically so that the value landscape has less diversity. However, on the 81 cells that *do* exhibit multi-core structure, family-core specialization is *higher* (0.738 vs. 0.59), indicating sharper family-core alignment when structural diversity survives. Family-conditioned field-max ratios (1.57 \times) and mean family-TV (0.117) match the primary pattern (1.55 \times , 0.135).

Table 19 72B replication summary. “Primary” is the pooled 3-model value cited in the main text; “72B” is the matched replication on the Qwen2.5-Math-72B-Instruct corpus.

Main construct	Primary (3-model)	72B	Conclusion
multi-core rate	67.6%	42.9%	attenuated by saturation
family \times core spec. (multi-core cells)	0.59	0.738	higher when multi-core
family / pooled-global field-max	1.55 \times	1.57 \times	matched
multi-correct-family rate	85.5%	67.3% (mean 3.18/prob)	attenuated by saturation
length-variance ratio	0.460	0.484	not a length artifact
mean family-TV	0.135	0.117	matched

Dataset-level values are included in Table 10. The overall pattern is that scaling from 8B to 72B attenuates multi-core and multi-family rates (via higher accuracy saturation), but preserves the qualitative atlas structure: when structural diversity survives, families specialize on disjoint core components even more sharply than at 8B.

E.2 Cross-Scale Replication on Qwen3-32B

We replicate the full canonical pipeline on Qwen3-32B (20,352 sampled runs; 318 non-code problems on AIME24/25, BRUMO25, GPQA, HMMT25) under the identical configuration. After degenerate-correctness filtering, 147 reward-evaluable cells remain.

Key result. Qwen3-32B closely matches the primary 3-model atlas picture and substantially outperforms the 72B replication on multi-family and multi-core rates. The multi-correct-family rate (89.6%) exceeds the primary headline (85.5%); multi-core rate (75.5%) matches Llama-8B (78.4%); family-TV (0.143) and family/global field-max (1.60 \times) are numerically matched to the primary (0.135, 1.55 \times). Unlike 72B, Qwen3-32B does not saturate on the math benchmarks, so the full multi-route structure is preserved at the 32B scale.

Table 20 Qwen3-32B replication summary.

Main construct	Primary (3-model)	32B	Conclusion
multi-core rate	67.6%	75.5%	matched / above
family \times core spec. (multi-core cells)	0.59	0.52	comparable
family / pooled-global field-max	1.55 \times	1.60 \times	matched
multi-correct-family rate	85.5%	89.6% (mean 4.64/prob)	matched / above
length-variance ratio	0.460	0.440	not a length artifact
mean family-TV	0.135	0.143	matched

E.3 Cross-Architecture Replication on DeepSeek-R1-Distill-Llama-8B

The Llama cross-architecture replication (16,512 runs across 258 problems on AIME24, AIME25, GPQA) is the strongest single piece of architecture transfer evidence. The same atlas picture reappears: multi-core solution landscapes, several correct-only families per problem, and near-identical family-core specialization.

Llama also matches the block-type localisation pattern of the reward field: its high-value landscape is answer-basin dominated (Table 12), and its family-level partition remains process-like rather than length-clustered. Family-TV dynamics replicate as well: across 152 Llama cells with valid typed-state kernels, 78.3% exceed the family-label shuffle null’s p_{95} , matching the primary rate of 80.9%. Taken together, the Llama replication shows that the atlas story is not tied to one architecture within the Qwen family.

Table 21 Llama-8B replication summary. “Primary” is the pooled 3-model value cited in the main text; “Llama” is the matched replication on the Llama corpus.

Main construct	Primary (3-model)	Llama	Conclusion
multi-core rate	67.6%	78.4%	multi-core dominant
family×core spec.	0.59	0.597	numerically matched
family / pooled-global field-max	1.55×	1.46×	matches sharpness
multi-correct-family rate	85.5%	78.3% (mean 3.98/prob)	multi-family dominant
length-variance ratio	0.460	0.469	not a length artifact
mean family-TV	0.135	0.127	matched
family-TV > null p_{95}	80.9%	78.3% ($n=152$)	matched